Research on Temperature Rise and Cooling System Optimization Design of Switched Reluctance Machine

Hao Chen, Yongqiang Liu, Fan Yang, Xing Wang, Zefu Tan, Li Cai, Antonino Musolino, Qian Huang, Yong Qi, Guanjun Wang, Lijun Xu, Kai Ge, Yokub Tairov, and Murat Shamiyev

***Abstract*—Excessive temperature rise during the operation of the generator system can affect the safety and life cycle of the machine. Therefore, in order to accurately obtain the internal temperature of the switched reluctance generator (SRG), an internal temperature estimation model based on electric heating is established in this paper. First, an improved variable coefficient Bertotti loss separation calculation formula is adopted to solve the iron loss of the generator under various operating conditions. Subsequently, the accurate heat source parameters in the temperature model can be obtained, and the corresponding heat source data can be calculated. Then, based on the obtained heat source data, an equivalent thermal circuit model is established for SRG. Meanwhile, in order to effectively reduce the internal temperature during SRG operation, a new water-cooled structure for direct cooling of SRG stator windings is proposed in this paper, which can effectively reduce the temperature rise during operation, thus improving the reliability of the generator. Finally, by comparing the equivalent thermal circuit model, finite element thermal model, and experimental temperature measurements of SRG, it is found that results from the equivalent thermal circuit model of the SRG are closer to the measured temperatures, while the effectiveness of the water-cooled structure is verified.**

***Index Terms*—Switched reluctance generator, junction temperature, finite element thermal model, equivalent thermal circuit model, water-cooled structure.**

I. Introduction

Energy shortages, climate warming, and environmental pollution are posing greater challenges to the automobile industry. The development of new energy and clean energy vehicles is being promoted by countries around the world to reduce carbon emission associated with traditional fossil fuel vehicles [1]–[3]. Many researchers have investigated the use of switched reluctance generators (SRMs) as the drive motors for electric vehicles, while SRMs also have a large potential for electric vehicle starting and power generation applications. Therefore, the operating performance of

Received: August 23, 2024
Accepted: March 26, 2025
Published Online: July 1, 2025

Hao Chen (corresponding author) is with the Shenzhen Research Institute, China University of Mining and Technology, Shenzhen 515100, China; the School of Electrical Engineering, China University of Mining and Technology, Xuzhou 221116, China; Xinjiang Institute of Engineering, Urumqi 830000, China; the International Joint Research Center of Central and Eastern European Countries on New Energy EV Technology and Equipment, Xuzhou 221008, China; the International Cooperation Joint Laboratory of New Energy Power Generation and EVs of Jiangsu Province Colleges and Universities, Xuzhou 221008, China; and the Xuzhou Key Laboratory of New Energy EV Technology and Equipment, Xuzhou 221008, China (e-mail: hchen@cumt.edu.cn).

Yongqiang Liu is with the School of Electrical Engineering, China University of Mining and Technology, Xuzhou 221116, China (e-mail: 860936052@qq.com).

Fan Yang is with the School of Electrical Engineering, Yancheng Institute of Technology, Yancheng 224000, China (e-mail: ts17130051a3@cumt.edu.cn).

Xing Wang is with the Shenzhen Research Institute, China University of Mining and Technology, Shenzhen 515100, China; and the International Joint Research Center of Central and Eastern European Countries on New Energy EV Technology and Equipment, Xuzhou 221008, China (e-mail: 3512@cumt.edu.cn).

Zefu Tan, Li Cai and Qian Huang are with the Department of Electrical Engineering, Chongqing Three Gorges University, Chongqing 400000, China (e-mail: 19930007@sanxiau.edu.cn; 20040001@sanxiau.edu.cn; 20150011@sanxiau.edu.cn).

Antonino Musolino is with the College of Engineering, University of Pisa, Pisa 56126, Italy (e-mail: antonino. musolino@unipi.it).

Yong Qi is with School of Computer Science and Engineering, Nanjing University of Science & Technology, Nanjing 210094, China (e-mail: 790815561@qq.com).

Guanjun Wang is with Wuxi Institute of Inspection, Testing and Certification, Wuxi 214101, China (e-mail: wgjcumt@126.com).

Lijun Xu is with Xinjiang Institute of Engineering, Urumqi 830000, China (e-mail: xulijun612@163.com).

Kai Ge is with the Automotive Engineering Research Institute, NAC, Nanjing 210000, China (e-mail: gekai@saicmotor.com).

Yokub Tairov and Murat Shamiyev are with the Faculty of Energy, Tashkent State Technical University, Tashkent 100095, Republic of Uzbekistan (e-mail: yokub.tairov.uzb@gmail.com; hellomurat2013@gmail.com).

DOI: 10.23919/PCMP.2024.000092

SRG for electric vehicles has gradually attracted the attention of researchers, especially its temperature rise characteristics [4]–[7]. Various losses are generated during the operation of SRG, resulting in temperature rises in various parts of the generator. The compact installation space and harsh interior environment make it difficult for SRG to dissipate heat, thereby exacerbating its local or overall temperature rise. Excessive temperature rise can directly affect the operational safety and lifespan of the generator. For example, excessive temperature rise may cause insulation damage between windings and lead to inter turn short circuits and other faults, which can seriously threaten the reliability and safety of the system. Therefore, studying the temperature rise characteristics and temperature rise suppression during SRG operation is of great significance.

To understand the temperature rise characteristics of the machine and identify the location of the high temperature point, it is necessary to calculate its temperature rise. The calculation also helps determine whether the temperature at the high temperature point exceeds the allowable upper limit for the material. There are two main methods for calculating the temperature rise of a machine: the analytical method and the numerical method. The analytical method involves the relevant theoretical equations, and the main analytical methods in thermal analysis are the equivalent thermal circuit method (ETCM) and the lumped parameter thermal network (LPTN). Numerical methods are used to solve any critical mathematical problem by using an iterative process until the solution converges. The main numerical methods used in thermal analysis are the finite element method (FEM) and computational fluid dynamics (CFD). In [8], an equivalent thermal resistance model is established to calculate the temperature rise in an induction motor by considering the effect of loading, and the analysis results are experimentally confirmed. In [9], temperature rises of a hybrid magnetization interior permanent magnet motor and a surface-mounted permanent magnet motor are compared by the analytical lumped-circuit method. Based on the obtained power losses, the lumped-parameter scheme is adopted to predict the temperature in each part of the flux-switching permanent-magnet double-rotor machine (FSPM-DRM) at hybrid driving mode in [10].

With the development and promotion of various commercial numerical analysis software, researchers can conduct more accurate temperature rise analysis and prediction of motors. In [11], a thermal equivalent circuit of the asymmetric H-bridge converter is established to obtain the junction temperature of power electronic devices. Based on the actual physical structure of the induction motor, a 3-D fluid-solid coupling transient model is built in [12], and the temperature distribution results during the starting process are analyzed when the induction motor starts with different loads. To obtain an accurate winding temperature gradient distribution of a tubular permanent magnet linear motor, a 2-D temperature field model is established in [13]. In [14], a co-simulation system of a permanent magnet synchronous motor (PMSM) finite element model and control system is built to compare the temperature rise simulation results of the PMSM under respective sine wave power supply and inverter power supply. In order to analyze the influence of voltage harmonics generated by the inverter on the loss and temperature of PMSM, a 2-D finite-element model is established in [15].

In addition, researchers have conducted extensive research on the temperature rise of SRM. In order to further improve the efficiency and power density of SRM, a simplified lumped parameter thermal network is applied in [16] to quickly evaluate the thermal behaviors of SRM based on the calculated iron loss. In [17], to establish the equivalent thermal circuit model conveniently, the mechanical structure of the machine is simplified and the characteristic nodes are divided. Then the heat transfer process in the rotor region, the stator region and the whole machine during the operation of the machine is analyzed, while the respective equivalent thermal circuit models of those regions are established. In [18], a mathematical calculation model of a four-phase 8/6 structure SRM is constructed to obtain the iron loss of each part of the machine. Then, the 2-D finite element thermal model and the experimental test platform of the SRM are established to analyze its temperature rise. In [19], a simplified 3D magneto-thermal model to study the temperature distribution over the housing of SRM is proposed. The main objective of the model is to study the temperature distribution profile on the body of the machine under various working conditions in order to introduce a temperature based signature to develop condition monitoring procedures. To calculate the temperature distribution in different parts of a 10 kW double-stator switched reluctance machine (DSSRM), a 3-D finite-element model is built and experimentally validated on the DSSRM prototype in [20].

The rest of this paper is organized as follows. In Section II, the basic principles of the SRG system are analyzed, and the SRG overall dynamic simulation model is established. The magnetic flux density waveforms and temperature rise heat sources of the SRG are calculated in Section III. In Section IV, the finite element thermal model and equivalent thermal circuit model of SRG are separately established, and their temperature rise calculation results are compared. Then, a novel water-cooled structure for direct cooling of the stator windings of the SRG is proposed in Section V. In Section VI, experiments are carried out to verify the temperature rise calculation results of the above two simulation models. Finally, Section VII concludes this paper.

II. Basic Principles of SRG System

Losses generated in SRG such as copper loss, iron loss, mechanical loss and stray loss are all heat sources leading to temperature rise of the generator. The calculation of various temperature rise heat sources of SRG is inseparable from various real-time parameters during the operation of the generator. Therefore, it is necessary to establish an overall SRG dynamic simulation model. The overall SRG model is mainly composed of logic controller module, power converter module, phase windings module and rotor angle calculation module. Figure 1 shows the principle block diagram of the structure of the overall SRG model, the information exchange between the modules and the direction of information exchange are also indicated. Based on the principle block diagram shown in Fig. 1, the overall dynamic simulation model of SRG is established in Matlab/Simulink, as shown in Fig. 2.

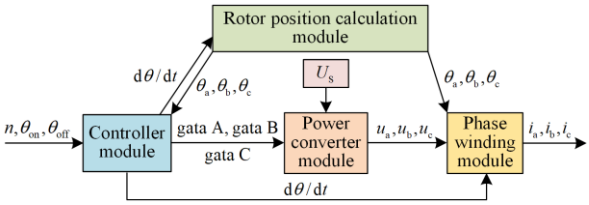

Fig. 1. Principle block diagram of SRG overall model.

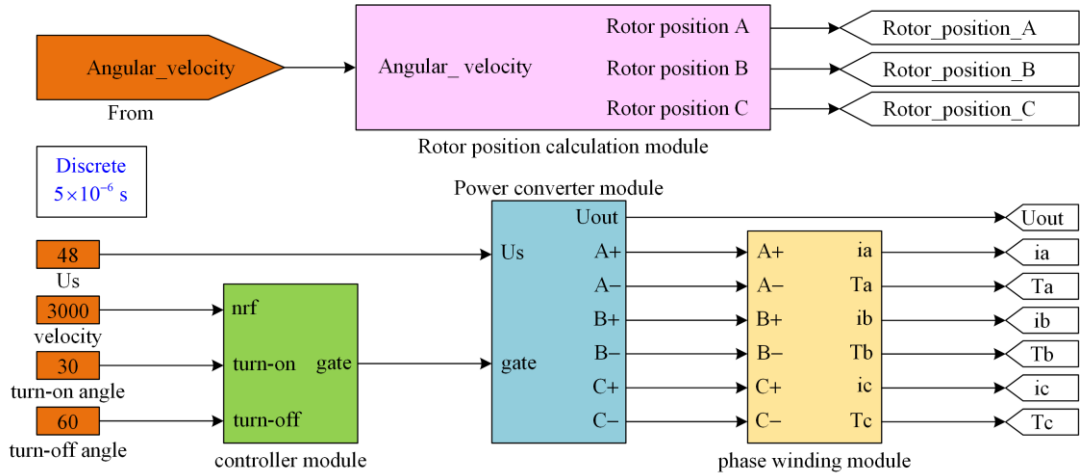

Fig. 2. SRG overall dynamic simulation model.

III. SRG Magnetic Density Characteristics and Heat Source Calculation

The various types of losses generated during the operation of the machine cause temperature rise, and among them, iron loss is one of the more difficult losses to solve accurately. Therefore, reasonable analysis and accurate calculation of iron loss is a prerequisite for accurate solution of SRG temperature rise. To calculate the iron loss of SRG, it is necessary to solve the magnetic flux density waveforms first. In this paper, a search method based on the static magnetic density is used to calculate the transient magnetic density at each characteristic point of the generator. Then, based on the solved transient magnetic density, an improved variable coefficient Bertotti loss separation calculation formula is used to solve the iron loss of the generator under various working conditions.

A. SRG Magnetic Density Solution

During the operation of SRG, due to its doubly salient structure and nonlinear magnetization curves of ferromagnetic material, the magnetic density waveforms of the generator present non-sinusoidal and nonlinear characteristics. In applications that require high accuracy and validity of magnetic density analysis results, researchers often use finite element analysis. Therefore, this paper establishes a 2-D finite element electromagnetic model of SRG to solve the static magnetic density in the working process of SRG.

According to the structural parameters and geometric dimensions of the SRG prototype shown in Table I, a finite element electromagnetic model of the SRG is established in the FLUX software. Its 2-D geometric surface domain is shown in Fig. 3, where the parts of the generator are labeled. During the operation of the SRG, different parts of the machine have different degrees of magnetic field saturation due to its doubly salient structure and nonlinear magnetization curves of the ferromagnetic material. Therefore, when solving the magnetic density of the SRG, it is necessary to divide the SRG surface domain and select the characteristic points according to the magnetic density distribution of each part of the generator. During the FEM analysis, it is found that the magnetic flux densities at the stator and rotor poles are high, especially when the rotor rotates to the position where the rotor pole overlaps the stator pole, and the magnetic field saturation at the tips of the stator and rotor poles is relatively high. For the stator and rotor poles where the magnetic lines of force pass through, the magnetic density distribution shows a weakening trend from the pole tip to the pole root. Accordingly, the SRG is divided into magnetic density regions as shown

in Fig. 3, and the center of each magnetic density region is selected as the characteristic point, which is also the location where the magnetic density sensor is placed and the static magnetic density is collected.

TABLE I
STRUCTURAL PARAMETERS AND GEOMETRIC DIMENSIONS OF THE SRG PROTOTYPE

Parameters	Symbols	Values
Shaft diameter (mm)	D_{sh}	20.00
Air gap (mm)	δ	0.30
Stator outer diameter (mm)	D_s	122.50
Rotor outer diameter (mm)	D_r	62.50
Stator yoke thickness (mm)	h_{sy}	11.00
Rotor yoke thickness (mm)	h_{ry}	11.00
Core thickness (mm)	L_{stk}	70.00
Stator pole arc angle	β_s	32.88
Rotor pole arc angle	β_r	34.69
Winding turns (turn)	N_c	72

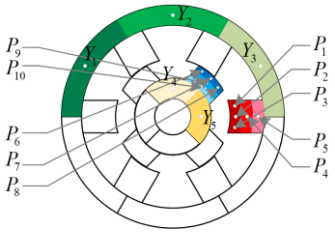

Fig. 3. Distribution positions of magnetic density sensors.

Considering the simultaneous existence of rotating magnetization and alternating magnetization in the working process of SRG, two magnetic density sensors are required to measure the tangential and radial components of the magnetic density respectively at one characteristic point. Moreover, in the working process of the three-phase SRG, the magnetic density at a characteristic point should be determined by considering the magnetic density generated by not only the main magnetic flux of the conducting phase, but also the leakage magnetic flux of the other two phases. Taking the characteristic point P_4 in the middle of the stator pole as an example, Figs. 4–6 show the static magnetic density waveforms of this characteristic point when phases A, B and C are separately energized.

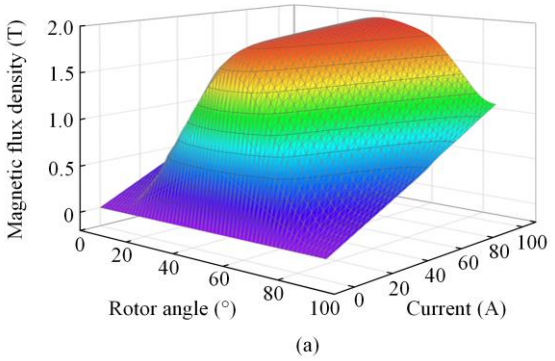

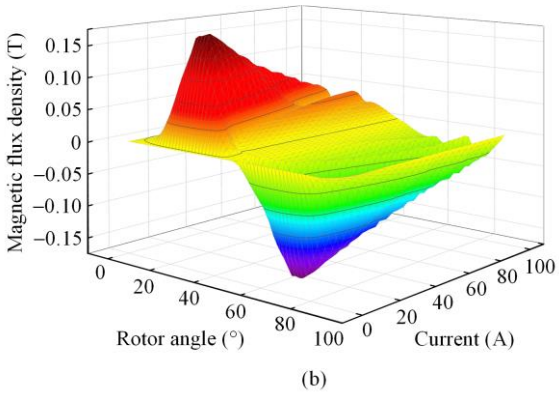

Fig. 4. Static magnetic density of point P_4 when phase A is energized. (a) Radial component of static magnetic density. (b) Tangential component of static magnetic density.

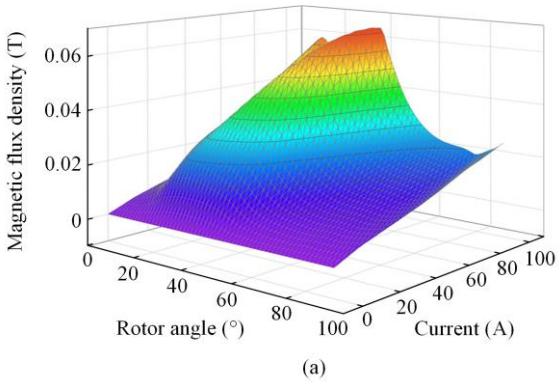

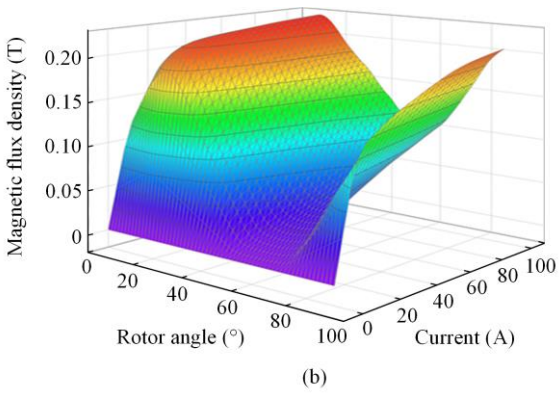

Fig. 5. Static magnetic density of point P_4 when phase B is energized. (a) Radial component of static magnetic density. (b) Tangential component of static magnetic density.

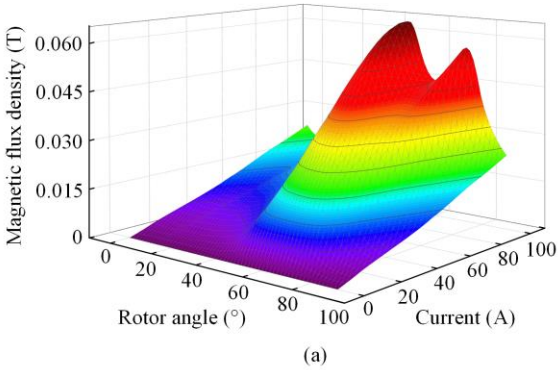

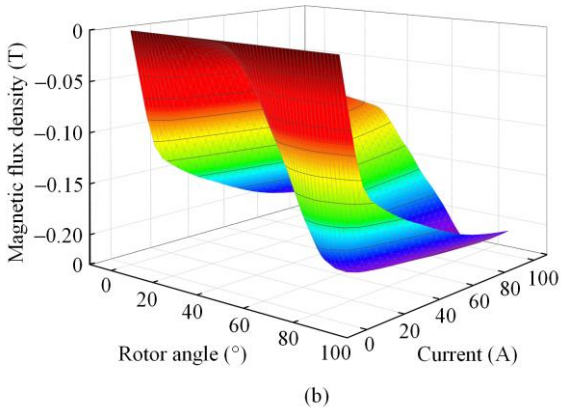

Fig. 6. Static magnetic density of point P_4 when phase A is energized. (a) Radial component of static magnetic density. (b) Tangential component of static magnetic density.

In this paper, the obtained static magnetic density data are imported into the transient magnetic density calculation module established in Matlab/Simulink. The transient magnetic density of the characteristic points is then calculated using the look-up table method. This method can adapt to the flexible conversion of multi-working conditions and has a short computational time. Taking the characteristic points of stator poles and rotor poles as examples, the transient magnetic density waveforms of these characteristic points are obtained by the method, as shown in Figs. 7 and 8.

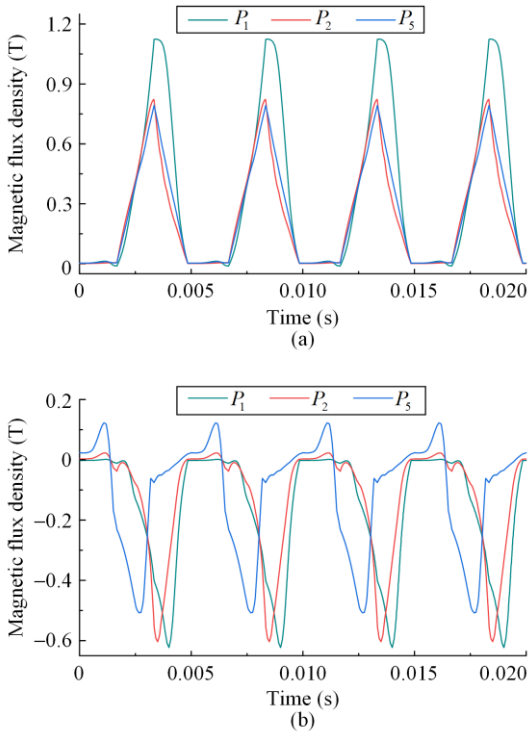

Fig. 7. Transient magnetic density waveforms of characteristic points of stator pole. (a) Radial component of transient magnetic density. (b) Tangential component of transient magnetic density.

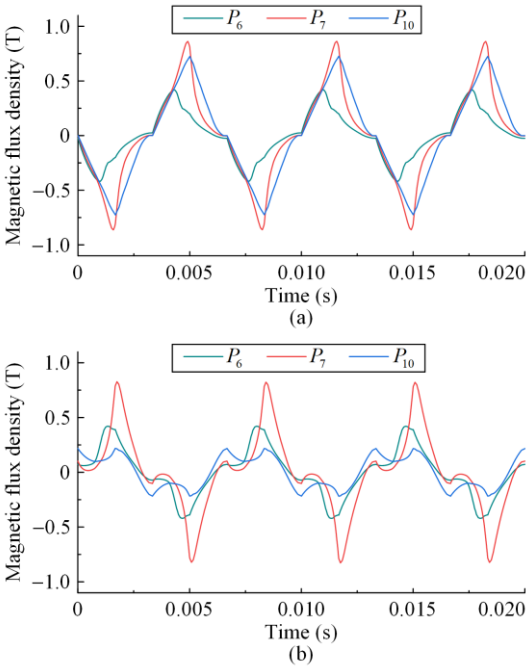

Fig. 8. Transient magnetic density waveforms of characteristic points of rotor pole. (a) Radial component of transient magnetic density. (b) Tangential component of transient magnetic density.

B. SRG Heat Sources Calculation

As an electromechanical energy conversion device, SRG inevitably produces various losses in various parts during the energy conversion process. Most of the losses generate heat, resulting in the temperature rise of various parts of the machine. Thus, accurate calculation of the various heat sources of SRG in the working process is a prerequisite for studying the temperature rise of SRG. According to the parts where the losses are concentrated in the SRG, it can be found that copper loss and iron loss occupy a large proportion of the total losses in the generator, and are the main heat sources causing the temperature rise.

In SRG, winding coils are only wound on the stator poles. When current flows through the stator windings, copper loss will be generated in the winding. Copper loss is the easiest to calculate of all the heat sources, and the copper loss P_{Cu} of a normal operating SRG can be calculated by:

$$P_{\mathrm{Cu}} = qI_{\mathrm{rms}}^2 R_{\mathrm{ph}} \tag{1}$$

where q is the number of phases of SRG and $q = 3$ for the prototype used in this study; R_{ph} is the resistance value of one phase of SRG winding; and I_{rms} indicates the root-mean-square (RMS) value of phase current.

Iron loss is the loss generated by the core material of the machine placed in a changing magnetic field, and its complex generation mechanism brings difficulties to the accurate solution of SRG iron loss. In this paper, the improved variable coefficient Bertotti loss separation computational formula is adopted to calculate SRG iron

loss. The computational expression of each variable coefficient is obtained by the fitting method, allowing for the establishment of a more accurate iron loss calculation model. At present, the iron loss separation model is a commonly used method, and in order to improve the classical three-term loss separation model with certain errors in the case of larger magnetic density peaks and higher frequency of magnetic density waveform changes, the variable coefficient three-term loss separation model is proposed in [21] and [22], and the computational expression is shown as follows:

$$P_{\mathrm{Fe}} = k_{\mathrm{ed}} B^2 f^2 + k_{\mathrm{hy}}(B) B^{n(B)} f + k_{\mathrm{ex}}(B, f) B^{1.5} f^{1.5} \quad (2)$$

where f is the frequency of magnetic density waveform variation; B is the motor magnetic density; $k_{\mathrm{hy}}(B)$ is the variable hysteresis loss coefficient; $n(B)$ is the variable Steinmetz coefficient; $K_{\mathrm{ex}}(B, f)$ is the variable additional loss coefficient related to both magnetic density and frequency; and k_{ed} is the eddy current loss coefficient.

In this paper, multiple measurements are carried out using the Epstein frame method on the silicon steel sheet material marked 35DW270, which is used in the prototype iron core. The iron loss data per unit mass of the silicon steel sheet material under different magnetic densities and frequencies are then obtained under the condition of a sinusoidal magnetic density waveform, as plotted in Fig. 9. By substituting the loss data shown in Fig. 10 into (2), and analyzing the variable coefficients in the equation and then using the data fitting method, the computational expressions of the variable hysteresis loss coefficient k_{hy}, the variable Steinmetz coefficient $n(B)$ and the variable additional loss coefficient k_{ex} shown in (3) can be obtained.

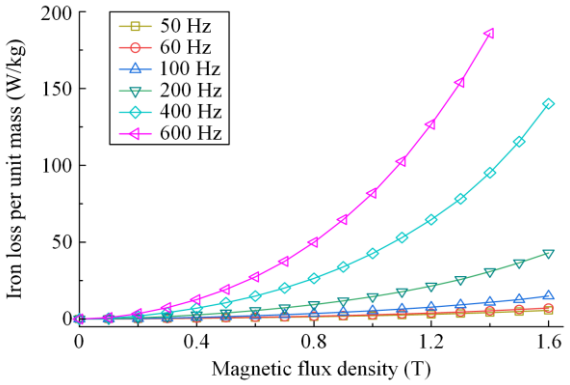

Fig. 9. Iron loss per unit mass at different frequencies.

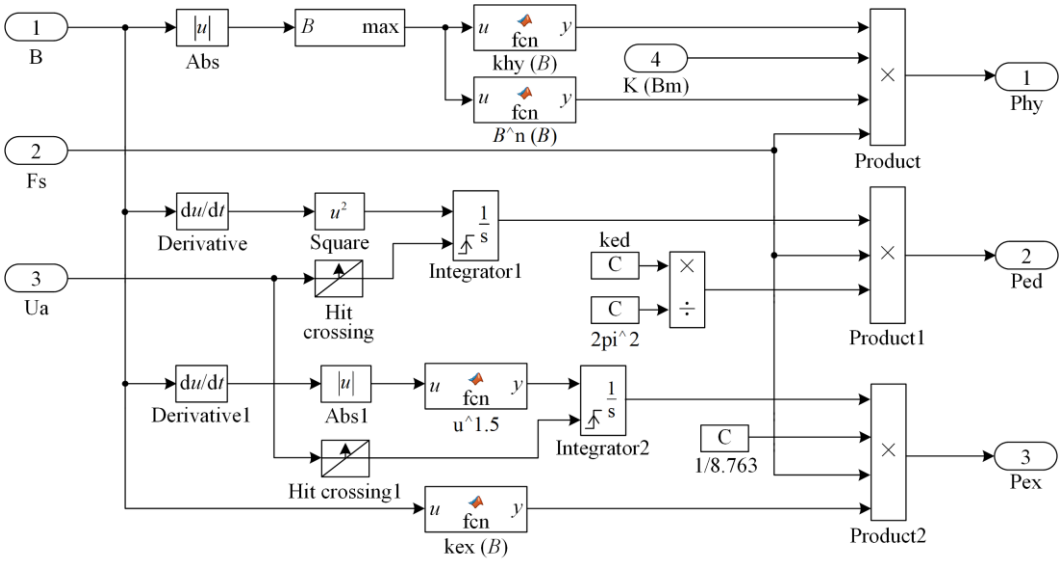

Fig. 10. SRG iron loss calculation basic model.

The iron loss calculation formula in (2) is only applicable to the case where the magnetic density waveform of the machine is sinusoidal, while SRG has a wide range of operating frequencies and operates with a non-sinusoidal magnetic density waveform. Based on the variable coefficients of the iron loss calculation model in (2), an improved iron loss separation calculation model suitable for all kinds of magnetic density waveforms is proposed in [23], which is also applicable to the iron loss calculation of SRG, given as:

$$P_{\mathrm{Fe}} = \frac{1}{T}\frac{k_{\mathrm{ed}}}{2\pi^2}\int_T \left(\frac{\mathrm{d}B}{\mathrm{d}t}\right)^2 \mathrm{d}t + \frac{1}{T} k_{\mathrm{hy}}(B_{\mathrm{m}}) B_{\mathrm{m}}^{n(B_{\mathrm{m}})} K(B_{\mathrm{m}}) + \frac{1}{T}\frac{k_{\mathrm{ex}}(B)}{8.763}\int_T \left|\frac{\mathrm{d}B}{\mathrm{d}t}\right|^{1.5} \mathrm{d}t \quad (3)$$

where T is the conduction period of one phase SRG; B_{m} is the peak magnetic density of motor; K_{hy} is the variable hysteresis loss coefficient; n is the variable Steinmetz coefficient; $K(B_{\mathrm{m}})$ is the hysteresis loss correction coefficient; and there are:

$$\begin{cases} k_{\mathrm{hy}}(B)=0.1131-0.06962\cos(1.359\mathrm{B})- \\ \qquad 0.09324\sin(1.359\mathrm{B})- \\ \qquad 0.01088\cos(2\times1.359\mathrm{B})+ \\ \qquad 0.02732\sin(2\times1.359\mathrm{B}) \\ n(B)=0.7137+2.356\cos(1.026\mathrm{B})- \\ \qquad 0.2714\sin(1.026\mathrm{B})- \\ \qquad 1.457\cos(2\times1.026\mathrm{B})- \\ \qquad 0.197\sin(2\times1.026\mathrm{B})+ \\ \qquad 0.1324\cos(3\times1.026\mathrm{B})+ \\ \qquad 0.1634\times\sin(3\times1.026\mathrm{B}) \\ k_{\mathrm{ex}}(B)=0.06313-0.01723\cos(1.207\mathrm{B})- \\ \qquad 0.08417\sin(1.207\mathrm{B})- \\ \qquad 0.02216\cos(2\times1.207\mathrm{B})+ \\ \qquad 0.008097\sin(2\times1.207\mathrm{B}) \end{cases} \tag{4}$$

According to (3) and (4), the basic calculation model of SRG iron loss is built in Matlab/Simulink, as shown in Fig. 10.

According to the previous loss analysis, the established SRG overall simulation model and loss model, and the loss heat source results of each part of SRG under different operating conditions, can be solved, as shown in Tables II–IV, where P_{sp}, P_{sy}, P_{rp}, P_{ry}, and P_{copper} represent the heat loss results of the stator poles, stator yokes, rotor poles, rotor yokes, and copper conductors, respectively.

TABLE II
HEAT SOURCE VALUES OF LOSS IN EACH PART OF SRG AT 2500 r/min

Turn-on condition	Main heat sources results of SRG				
Angles	P_{sp} (W)	P_{sy} (W)	P_{rp} (W)	P_{ry} (W)	P_{copper} (W)
27°–60°	26.72	41.36	15.45	16.67	99.45
30°–57°	22.79	34.87	11.41	15.22	83.61
30°–60°	25.02	39.45	12.45	16.21	92.93
30°–63°	29.77	43.29	17.09	18.80	112.87
33°–60°	23.47	34.13	12.18	14.83	87.82

TABLE III
HEAT SOURCE VALUES OF LOSS IN EACH PART OF SRG AT 3000 r/min

Turn-on condition	Main heat sources results of SRG				
Angles	P_{sp} (W)	P_{sy} (W)	P_{rp} (W)	P_{ry} (W)	P_{copper} (W)
27°–60°	23.67	39.28	14.32	15.52	90.33
30°–57°	19.37	30.92	11.51	13.85	78.51
30°–60°	22.96	36.06	12.29	14.82	85.42
30°–63°	26.10	40.83	15.14	17.57	97.64
33°–60°	20.03	30.38	11.31	13.95	81.75

TABLE IV
HEAT SOURCE VALUES OF LOSS IN EACH PART OF SRG AT 4000 r/min

Turn-on condition	Main heat sources results of SRG				
Angles	P_{sp} (W)	P_{sy} (W)	P_{rp} (W)	P_{ry} (W)	P_{copper} (W)
27°–60°	20.14	34.96	11.33	13.02	77.31
30°–57°	14.51	25.69	8.62	10.74	68.93
30°–60°	17.59	31.22	10.02	12.05	74.16
30°–63°	20.46	36.48	13.11	16.24	82.37
33°–60°	14.98	26.56	8.82	11.02	71.42

IV. SRG TEMPERATURE RISE SOLUTION MODELS

During operation, various losses are generated in SRG, resulting in the rise of generator temperature. The insulation performance of the winding structure will be affected by excessive temperature rise, thereby impacting the operational reliability and safety of the generator. Therefore, it is necessary to analyze the temperature field distribution and temperature rise characteristics of SRG. The commonly used methods for analyzing temperature field include simplified formula method, finite element method and equivalent thermal circuit method. However, the simplified formula method can no longer meet the requirements of accurately analyzing the machine temperature field. In this section, based on the heat sources calculated above, and according to the actual dimensions and materials of the SRG prototype, the 3-D finite element thermal model of the SRG is established in the software FLUX, while an equivalent thermal circuit model of the SRG is established in the motor thermal design software Motor-CAD. Then, the temperature rise of the SRG is solved separately in the two models, and the simulation results are compared and analyzed.

The prototype studied in this paper is a three-phase 6/4 structure SRG with water-cooled channels, and the overall structure and radial cross section of the generator are shown in Fig. 11. It can be seen that the water-cooling structure of the SRG prototype consists of an axial spiral water channel with a rectangular cross-section, and the water-cooling channels are wrapped around the outside of the motor core, providing effective cooling of the generator. As shown in Fig. 12, the generator prototype is mainly composed of the end caps, the shaft, the rotor core, the windings, the stator core and the water-cooled shell. A fully enclosed structure is adopted by the SRG prototype, so the machine is forced to be water-cooled using the cooling water circulating in the water-cooling channels.

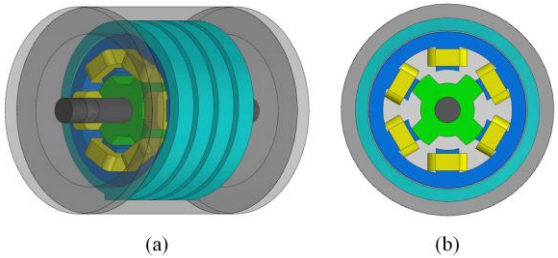

Fig. 11. Structure diagram of the water-cooled SRG. (a) SRG overall structure diagram. (b) SRG radial cross section.

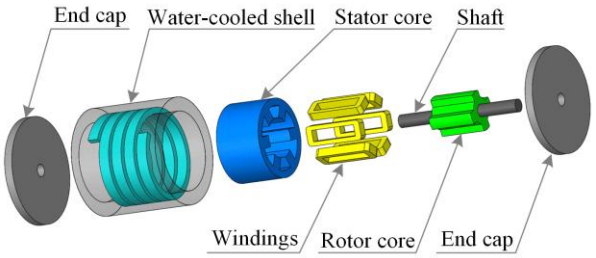

Fig. 12. Mechanical composition analysis diagram of the water-cooled SRG.

A. SRG Finite Element Thermal Model

Based on the structural composition of the SRG prototype shown in Fig. 13 and the geometry dimensions given in Table I, a 3-D finite element thermal model of the water-cooled SRG is built in the FLUX software. In order to facilitate the temperature field analysis and simplify the temperature rise calculation, the stator winding is equivalent to two parts, i.e., the equivalent copper conductor and the equivalent insulation layer. In order to calculate the exact temperature rise of each part of the SRG core, the core region is split into stator pole region, stator yoke region, rotor pole region and rotor yoke region.

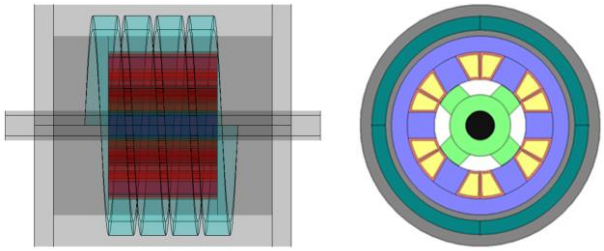

Fig. 13. 3-D finite element thermal model of the water-cooled SRG. (a) Overall structure. (b) Radial section.

In addition, boundary condition setting is an important part of building the SRG finite element thermal model. In the SRG finite element thermal model, the interface between the generator shell and the external air can be described by the first boundary condition, whereas the inner wall of the cooling water channel in the water-cooled housing can be described by the second boundary condition.

According to the previous loss analysis, taking the working condition of SRG at 3000 r/min as an example, the data of each heat source is imported into the corresponding area of the SRG finite element thermal model, and the temperature field distribution of the generator can be obtained after the solution. The temperature field distribution after the solution of the SRG finite element thermal model without and with water-cooled measure at the ambient temperature of 20 ℃ are shown in Figs. 14 and 15, respectively. It can be seen from Fig. 14 that the stator winding is the part with the highest temperature rise of the SRG. Under this condition, the maximum temperature of the SRG without water-cooled measure is 81.3 ℃.

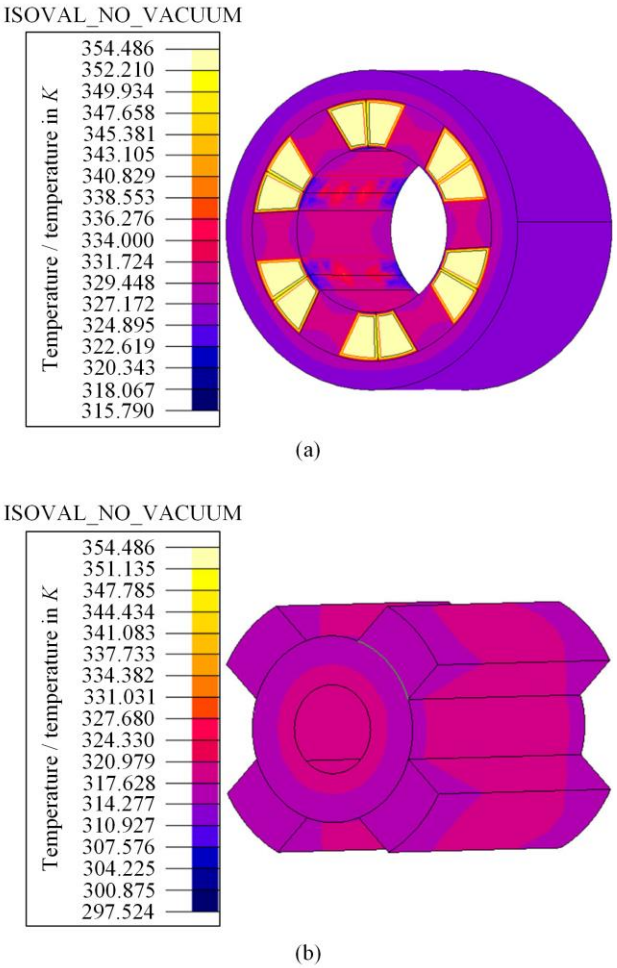

Fig. 14. Temperature field distribution of common SRG finite element thermal model. (a) Temperature field distribution of stator part. (b) Temperature field distribution of rotor part.

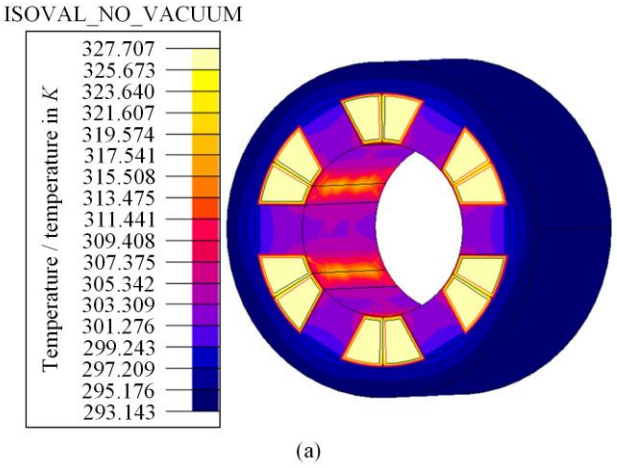

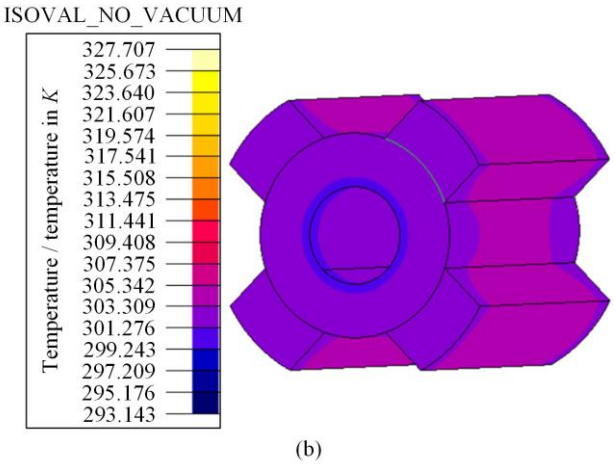

Fig. 15. Temperature field distribution of water-cooled SRG finite element thermal model. (a) Temperature field distribution of stator part. (b) Temperature field distribution of rotor part.

From Fig. 15, it can be found that the part with the highest temperature rise of the SRG is still the stator winding, and the maximum temperature of the SRG with water-cooled measure is 54.6 ℃. The maximum temperature of the generator is reduced by 26.7 ℃ when the water-cooled condition is added in the system, which can effectively cool down the generator.

From the temperature field distribution of the stator part, it can be seen that the temperature rise of the stator winding part is higher, which indicates that the copper loss generated by the SRG during power generation is large. In the radial direction, an obvious temperature distribution gradient is observed in the stator pole part, especially under the water-cooling condition. The reason is that, since the SRG structure is closed, the internal heat dissipation conditions are poor, and the heat conduction from the winding part results in a higher temperature in the stator pole part. Therefore, the heat is conducted to the lower temperature stator yoke, forming a temperature gradient. In the axial direction, due to the better heat dissipation conditions at the ends of the stator part, the axial temperature distribution of the stator poles presents the characteristics of high in the middle and low on both sides. From the temperature field distribution of the rotor part, it can be observed that the rotor part also exhibits characteristics of temperature distribution in the radial and axial directions. The highest temperature of the rotor core part is located inside the rotor yoke, while the lowest temperature is located at the axial end face of the rotor. The iron loss heat source of the SRG rotor part is small, and because it is located inside the SRG and has no direct and effective heat dissipation measures, the temperature gradient of the SRG rotor part is small.

The heat source data in Tables II–IV are imported into each part of the water-cooled SRG 3-D finite element thermal model, allowing the temperature rise under different working conditions of each part of the generator to be determined, as shown in Tables V–VII, where T_{sp}, T_{sy}, T_{rp}, T_{ry} and T_{copper} respectively represent the temperature rises of the stator poles, stator yoke, rotor poles, rotor yoke and copper conductor of the SRG.

The temperature rise data in Tables V–VII shows that the stator winding part of the SRG always has the highest temperature rise in all operating conditions because of the high copper loss heat source in the winding part, while the stator yoke part of the SRG always has the lowest temperature rise due to the forced convection heat dissipation by the cooling water in the housing. The temperature rise of the same part of the generator decreases with the increase of the speed of the SRG when the turn-on and turn-off angles are constant. This is because the RMS value of the generating current decreases with the increase of the speed, which leads to the decrease of the copper loss. In addition, with the increase of the conduction angle when the generation speed is constant, the RMS value of the generation current increases so the temperature rise of the same part of the generator also increases.

TABLE V
TEMPERATURE RISE OF EACH PART OF SRG WITH FINITE ELEMENT THERMAL MODEL AT 2500 r/min

Turn-on condition	Main heat sources results of SRG				
Angles	T_{sp} (℃)	T_{sy} (℃)	T_{rp} (℃)	T_{ry} (℃)	T_{copper} (℃)
27°–60°	23.5	16.2	28.1	28.4	54.1
30°–57°	19.1	13.1	20.3	20.5	38.4
30°–60°	21.8	15.2	24.8	25.1	47.8
30°–63°	25.7	17.4	33.2	33.6	60.1
33°–60°	20.4	14.0	22.1	22.3	43.5

TABLE VI
TEMPERATURE RISE OF EACH PART OF SRG WITH FINITE ELEMENT THERMAL MODEL AT 3000 r/min

Turn-on condition	Main heat sources results of SRG				
Angles	T_{sp} (℃)	T_{sy} (℃)	T_{rp} (℃)	T_{ry} (℃)	T_{copper} (℃)
27°–60°	20.4	13.8	23.2	23.7	46.8
30°–57°	16.5	11.7	18.0	18.2	34.2
30°–60°	18.8	12.9	21.4	21.8	38.7
30°–63°	21.7	14.9	25.4	25.9	48.8
33°–60°	17.2	12.1	19.1	19.4	35.6

TABLE VII
TEMPERATURE RISE OF EACH PART OF SRG WITH FINITE ELEMENT THERMAL MODEL AT 4000 r/min

Turn-on condition	Main heat sources results of SRG				
Angles	T_{sp} (℃)	T_{sy} (℃)	T_{rp} (℃)	T_{ry} (℃)	T_{copper} (℃)
27°–60°	19.2	13.1	20.5	20.7	38.7
30°–57°	15.1	10.9	15.7	15.9	26.8
30°–60°	17.4	12.2	18.1	18.4	30.4
30°–63°	20.9	13.9	23.0	23.3	41.5
33°–60°	15.7	11.3	16.9	17.1	29.7

B. SRG Equivalent Thermal Circuit Model

Motor-CAD is a professional motor thermal design software based on the equivalent thermal circuit method for thermal analysis and optimization design of motors, and its magneto-thermal mutual coupling analysis function can accurately calculate the temperature rise of the motor. The motor temperature rise is mainly related to two factors. One is the various heat sources of the motor, as various losses are inevitably generated during the operation of the motor, and the other is the cooling performance of the motor, which is mainly related to the cooling method and heat dissipation structure.

The various cooling methods, heat dissipation structures and cooling media contained in the Motor-CAD software provide convenience for the improvement of motor cooling performance. Based on the dimensional parameters in Table I, a 3-D geometric model of the SRG is established in the Motor-CAD software, as shown in Fig. 16. The software automatically generates the equivalent thermal circuit shown in Fig. 17 based on the established SRG geometry model.

In the equivalent thermal circuit, several temperature nodes representing the critical parts of the SRG are provided, and these temperature nodes are connected to the various thermal resistances and heat sources to form a complete thermal circuit. Based on the key temperature nodes, the software automatically analyzes and calculates the thermal resistance values between the nodes. Finally, the temperature values of each temperature node are calculated by injecting the corresponding heat source data into the heat source node.

Taking the working condition of SRG at 3000 r/min as an example, the data of each heat source are imported into the SRG equivalent thermal circuit model, and the temperature field distribution of the generator is obtained after the solution. The temperature field distribution of the axial section after the solution of the SRG equivalent thermal circuit model with water-cooled measure at the ambient temperature of 20 ℃ is shown in Fig. 18. The temperature field distribution characteristics of the SRG obtained by the equivalent thermal circuit model are consistent with the results obtained by the finite element thermal model, and are not be repeated here. The heat source data in Tables II–IV are respectively imported into the water-cooled SRG equivalent thermal circuit model, and the temperature rise results of each part of the generator under different working conditions can also be obtained.

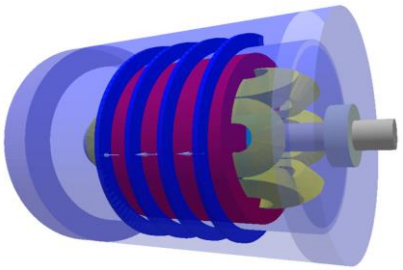

Fig. 16. 3-D diagram of water-cooled SRG.

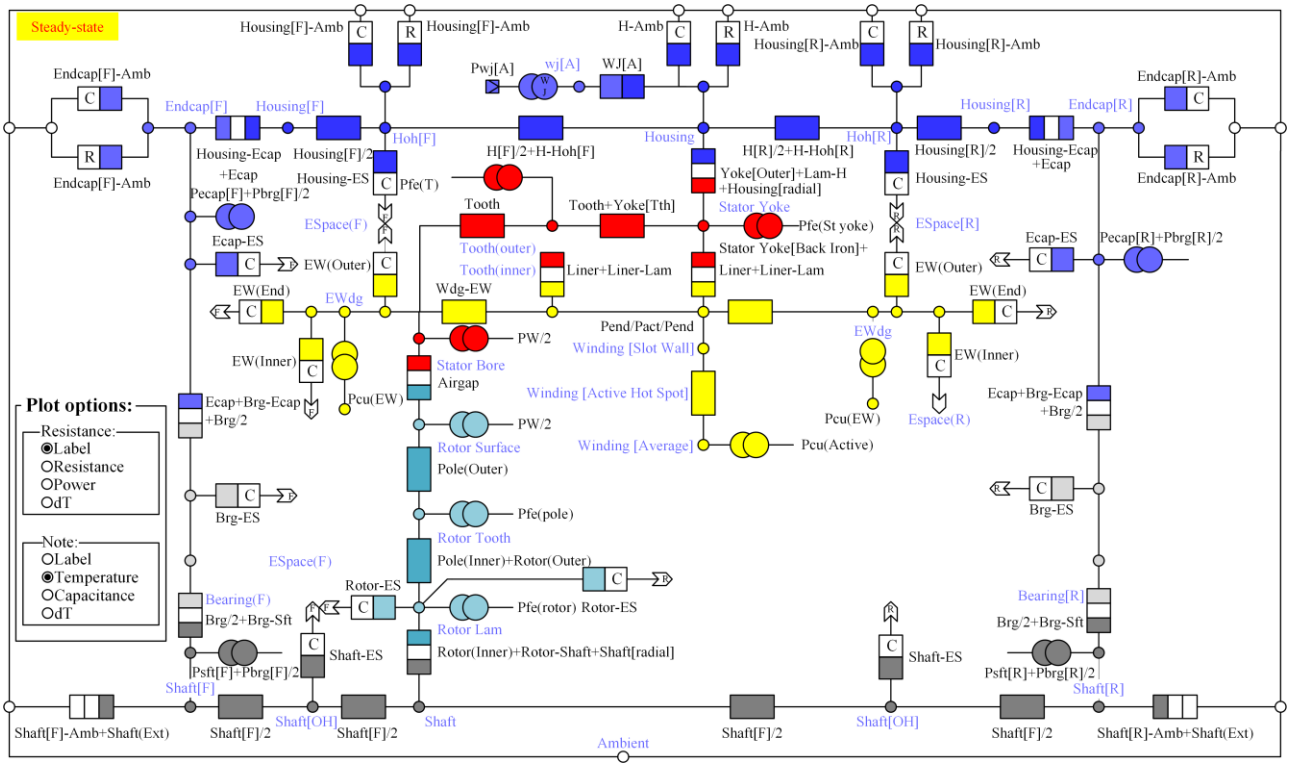

Fig. 17. Equivalent thermal circuit diagram of water-cooled SRG.

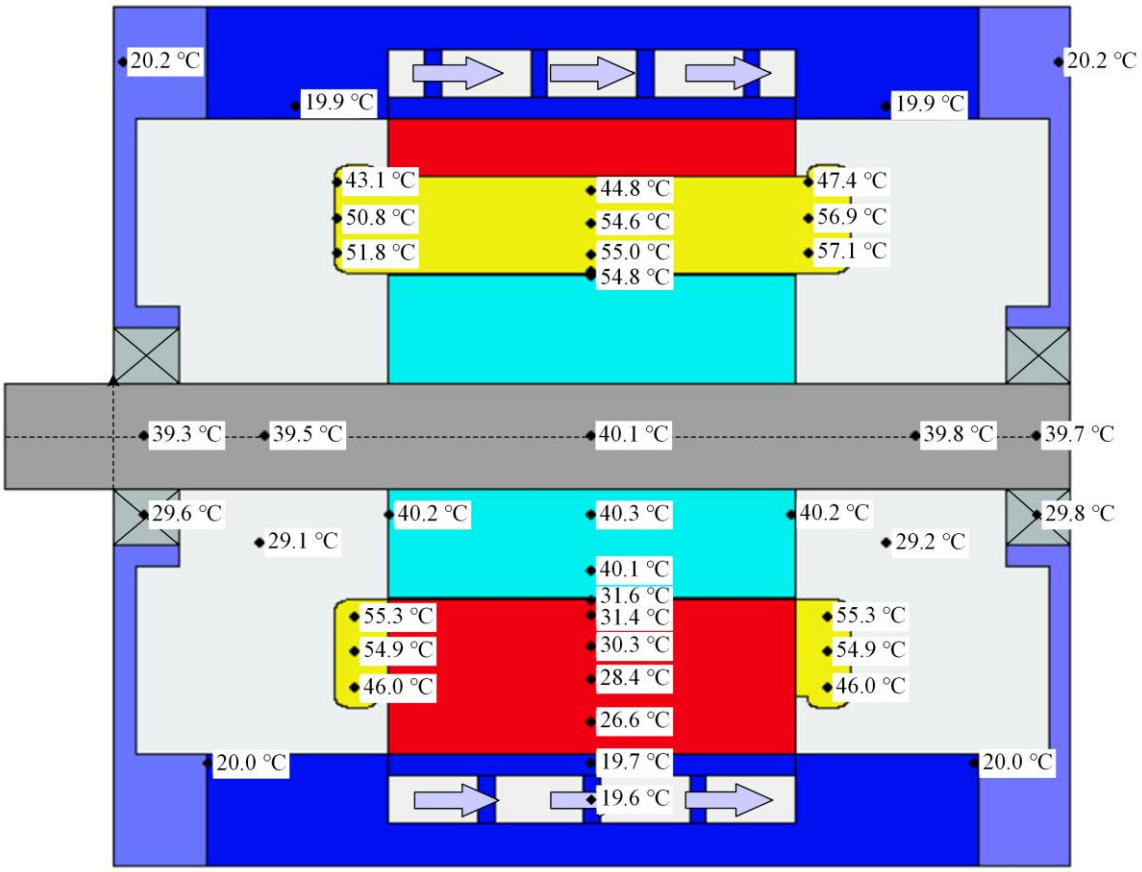

Fig. 18. Axial section temperature field distribution of water-cooled SRG thermal model.

C. Comparison of SRG Temperature Rise Simulation Results

In order to further compare the calculation effects of the two temperature rise calculation models, the temperature rise results obtained from the parts with higher temperature rise are selected in this paper to compare and verify the two methods. The comparative histograms of the temperature rise results from the finite element thermal model and the equivalent thermal circuit model for the winding part of the SRG with the highest temperature rise, the rotor yoke part with the higher temperature rise in the rotor core, and the stator pole part with the higher temperature rise in the stator core are presented in Fig. 19 under different speeds of the SRG at the respective turn-on and turn-off angle of 30° and 63°.

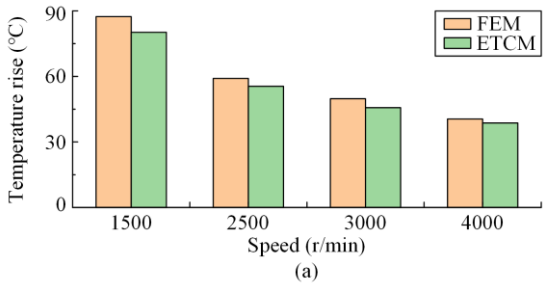

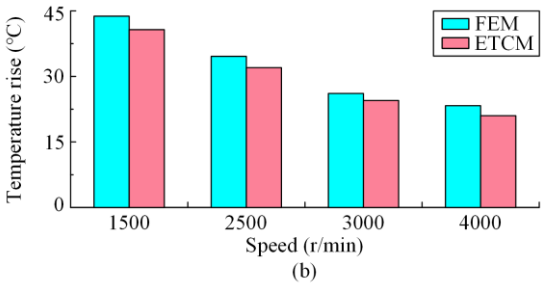

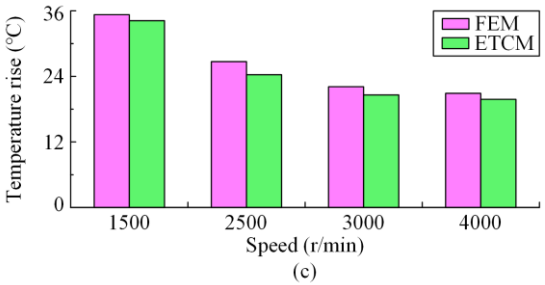

Fig. 19. Comparison of temperature rise calculation results between the finite element thermal model and equivalent thermal circuit model of SRG. (a) Winding temperature rise results. (b) Rotor yoke temperature rise results. (c) Stator pole temperature rise results.

According to the comparison of the temperature rise results in Fig. 19, it can be more intuitively found that when the turn-on and turn-off angles are constant, the

temperature rise results solved by the finite element thermal model and the Motor-CAD equivalent thermal circuit model both decrease with the increase of the rotational speed. By comparison, the temperature rise results obtained by the finite element thermal model are higher, and the maximum deviations by the two simulation thermal models of the winding part, the rotor yoke part and the stator pole part are 7.2 ℃, 3.1 ℃ and 2.4 ℃ respectively. Therefore, it can be seen that the results obtained by the two temperature rise solution models have a larger deviation in the winding part. The deviation of the two methods is mainly due to the difference of the solution characteristics between the finite element method and the equivalent thermal circuit method. The 3-D SRG model is divided into many sub-elements by the finite element method, with the size of the divided elements affecting the solution results. Additionally, the setting of the boundary conditions of the finite element thermal model also affects the SRG temperature rise calculation results to a certain extent. The equivalent thermal circuit method uses the idea of "transforming the field problem into a circuit problem", and certain assumptions are used in the process of establishing the thermal circuit, while the temperature node can only reflect the average temperature of the area, which will cause the deviation of calculated temperature rise. The temperature rise results calculated by the two methods need to be further verified by experiments. However, in general, the temperature rise results solved by the finite element thermal model and the Motor-CAD equivalent thermal circuit model are fairly close, and the two methods have been verified by each other.

V. Optimization Design of SRG Water-cooling System

In order to suppress the excessive temperature rise of SRG during operation, reasonable and effective cooling measures are required. A high convective heat transfer coefficient is associated with the water-cooled form, so the water-cooled system is commonly used as an effective cooling measure for motors. The structure of cooling water channel in the water-cooling system is directly related to the fluid state of the cooling water and the convective heat transfer area between the cooling water and the inner wall of the cooling channel, which is an important factor affecting the cooling effect of the water-cooling system and an important aspect of the water-cooling system design. The water-cooling structure of the SRG prototype in this paper is a spiral water-cooled structure arranged inside the housing. The SRG can be effectively cooled by this arrangement, but direct cooling of the winding part, which has a high temperature rise, is difficult. When the SRG is assembled, there is an approximately inverted triangle-shaped gap in the middle of the stator slot, as shown in Fig. 20. Combining the characteristics and dimensions of the gap inside the stator slot and taking into full consideration the thermal expansion of the winding, a new water-cooled structure is proposed in this paper which can effectively cool down the winding part of the generator, as shown in Fig. 21.

Fig. 20. Assembly diagram of stator windings.

Fig. 21. Winding direct cooling water-cooling structure. (a) Overall structure. (b) Radial section.

As shown in Fig. 21, the new water channel passes through the middle of the stator slot, bypasses the end winding and enters another stator slot, thus completing the cooling of all stator windings. The new water channel can be composed of the slot water channel and the end water channel. The slot water channel can cool the windings in the slots, and the end water channel can cool not only the adjacent end windings, but also the air at both ends inside the generator. In addition, the end water channel with the arched structure is also beneficial to reduce the water resistance during the flow of cooling water. The cross section of the new water channel is approximately trapezoidal, and full contact with the stator yoke is made by its upper side wall, which is conducive to effective cooling of the stator yoke. The contact area with the winding part is increased by its rectangular side surface. However, a more complicated manufacturing process will be required for this new water-cooling channel.

For the winding direct cooling water-cooled structure shown in Fig. 21, a 3-D thermal model of the SRG with the new water-cooled structure is built in FLUX, and the thermal model is solved after importing the heat source data at 3000 r/min, while the temperature field distribution after the solution is shown in Fig. 22. Comparing the calculation results of the SRG temperature field of the new water-cooled structure in Fig. 22 with that of the spiral water-cooled structure in Fig. 15, it can be found that the temperature of the winding part of the

SRG with the new water-cooled structure is reduced by 8.53 ℃. Less effect on the temperature field of the rotor part is caused by the change of the water-cooled structure. Due to the lack of water-cooled channel in the housing, the temperature of the stator core part rises by about 3–5℃. The cooling effectiveness of the new water-cooling structure for direct cooling of the windings is proven by the comprehensive comparison.

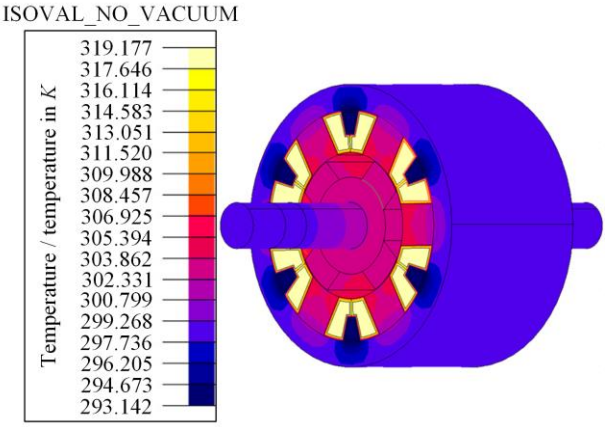

Fig. 22. Temperature field distribution of the new water-cooled SRG finite element thermal model.

VI. Experimental Verification

In order to verify the accuracy of the temperature rise calculation results of the finite element thermal model and the equivalent thermal circuit model, the temperature rises of the key parts of the SRG prototype during operation are experimentally measured. In the process of motor temperature rise experiments, the commonly used temperature measurement methods include thermometer method, resistance method and detector buried measurement method. According to the simulation models, the winding area is where the highest temperature rise of the water-cooled SRG studied in this paper occurs. The thermocouple sensors and the stator windings have been wound together during the fabrication of the SRG prototype, as shown in Fig. 23, and the detector buried measurement method is adopted to measure the winding temperature during the operation of the SRG in the experiments.

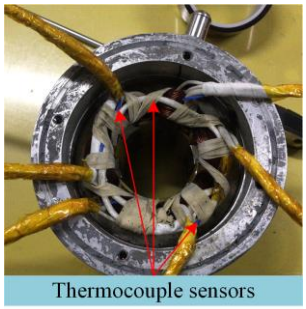

Fig. 23. Embedding position of thermocouple sensors.

A. Experimental Platform

The experimental platform used for the SRG temperature rise measurement is shown in Fig. 24, which mainly consists of a hardware circuit platform and a three-phase 6/4 structure water-cooled SRG unit platform. The SRG is rated at a speed of 3000 r/min and a power of 500 W. The power converter is a three-phase asymmetric half-bridge topology, and the separate excitation method is adopted with an excitation voltage of 48 V.

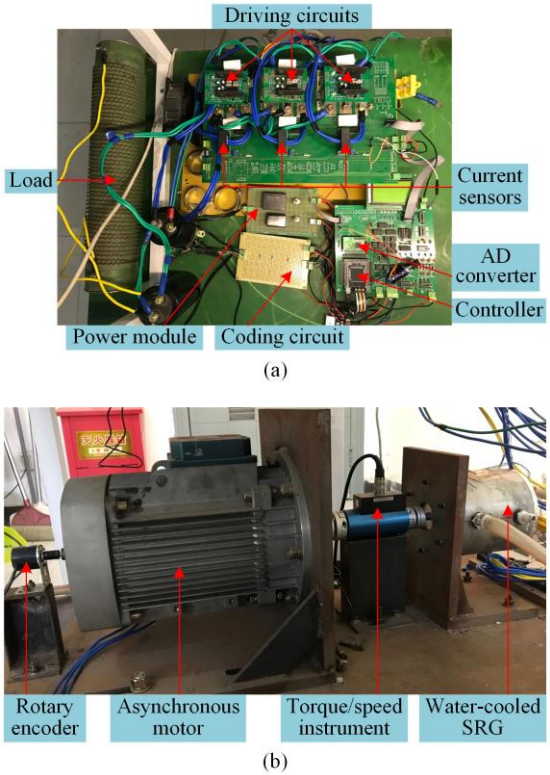

Fig. 24. SRG power generation experimental platform. (a) Hardware circuit platform. (b) SRG unit platform.

The SRG prototype used in the experiments adopts the forced water-cooling method, and the cooling water circulates through the spiral cooling water channel in the housing to continuously cool the SRG. The experimental water-cooling system is shown in Fig. 25.

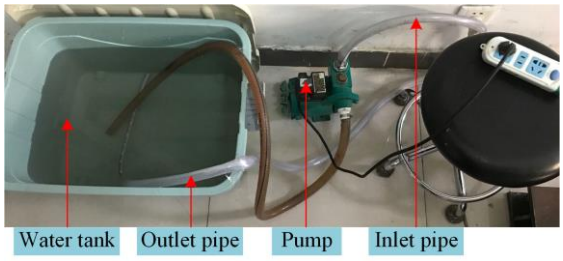

Fig. 25. SRG water-cooling system.

Due to the limited space in the experimental site, the realization of circulating water-cooling during the op-

eration of the SRG is achieved using a water pump and a water tank, with the flow rate of the existing water pump in the laboratory being 33 L/min. Before the SRG starts to generate power driven by the asynchronous motor, the water pump is started first, so that the SRG can keep working in the water-cooled state. Therefore, the temperature data measured in the experiments is the average temperature of the SRG windings under the water-cooling measures.

The temperature rise measurement platform of the water-cooled SRG is shown in Fig. 26. The real-time temperature data of the stator windings can be read by connecting the thermocouple sensors to the temperature inspection instrument.

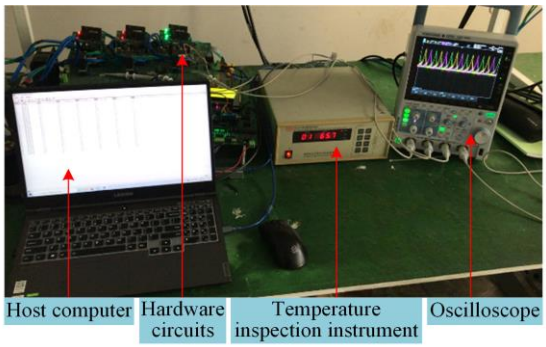

Fig. 26. SRG temperature rise measuring platform.

B. Temperature Rise Measurement Results of SRG Windings

In order to verify the accuracy of the overall dynamic simulation model of the SRG established above, the three-phase generation current waveforms i_A, i_B, i_C and load current waveform i_L obtained from the simulations are compared with the corresponding current waveforms from the experiments, as shown in Figs. 27 and 28, under the speed of 1500 r/min and the conducting condition of 30°–60°. From Figs. 27 and 28, it can be found that the current waveforms obtained by simulations and by experiments are relatively consistent, which provides a good basis for the subsequent calculation of the SRG heat sources and temperature rise.

In this water-cooled SRG temperature rise test, the temperature rise results of the SRG are measured under the speed of 2500 r/min, 3000 r/min and 4000 r/min, respectively. The experimental temperature rise curves of the stator windings for the corresponding speed cases are given in Figs. 29–31. Since the selection of the turn-on and turn-off angles has a large impact on the RMS value of the power generation current, which further affects the SRG copper loss, the temperature rise curves are measured for each speed case when the turn-on and turn-off angles are 27°–60°, 30°–57° and 30°–60°, respectively. According to the three sets of temperature rise curves of the windings, it can be seen that the temperature rise of the SRG windings decreases with the increase of the rotational speed when the turn-on and turn-off angle are constant. When the speed of the SRG is constant, the temperature rise of the windings is higher within a certain range with a larger conduction angle.

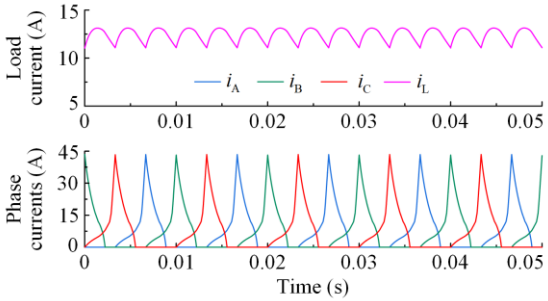

Fig. 27. Simulated current waveforms of SRG at 1500 r/min.

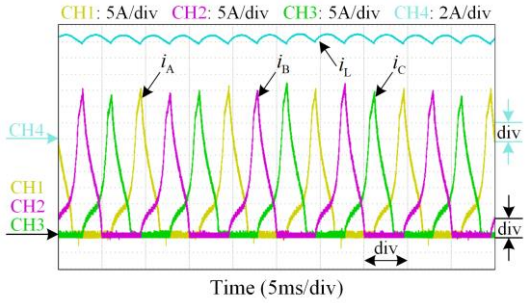

Fig. 28. Experimental current waveforms of SRG at 1500 r/min.

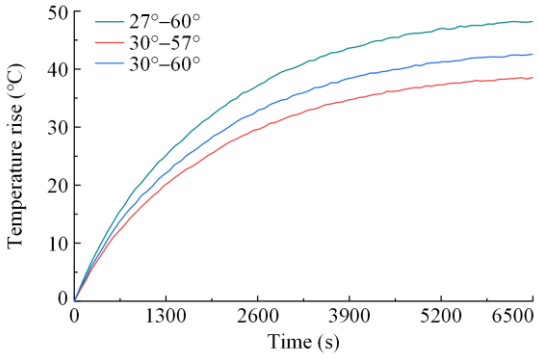

Fig. 29. Temperature rise curves of SRG windings at 2500 r/min.

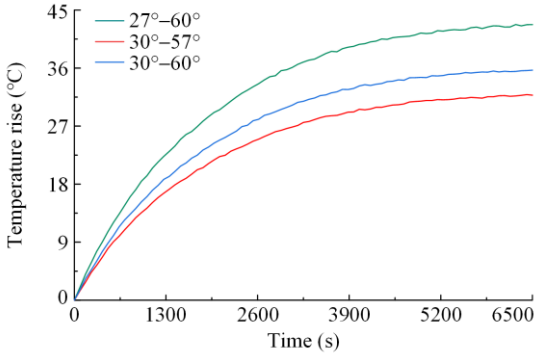

Fig. 30. Temperature rise curves of SRG windings at 3000 r/min.

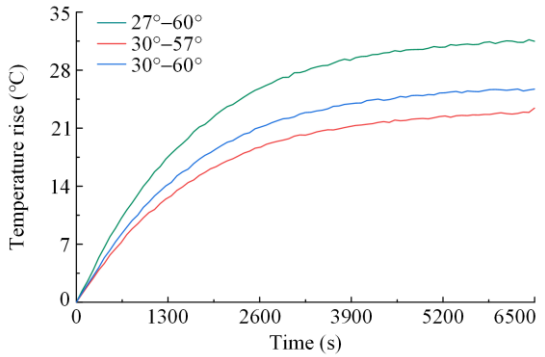

Fig. 31. Temperature rise curves of SRG windings at 4000 r/min.

C. Comparison of SRG Windings Temperature Rise Results

The experimentally measured windings temperature rise results are compared with those calculated by the 3-D finite element thermal model and the equivalent thermal circuit model under different operating conditions, as shown in Figs. 32(a), (b) and (c) under the turn-on and turn-off angles of 27°–60°, 30°–57° and 30°–60°, respectively. It can be found from Fig. 32 that, the variation trends of the winding temperature rise results by the 3-D finite element thermal model, the equivalent thermal circuit model and the experiments, under different working conditions, are consistent. Among them, the temperature rise calculation results of the SRG finite element thermal model has larger deviations from the measured results, but the maximum error does not exceed 6.2 ℃, while the temperature rise calculation results of the Motor-CAD equivalent thermal circuit model are close to the measured values. In general, the calculated results of the Motor-CAD equivalent thermal circuit model are considered more accurate, with the maximum error between the 3-D finite element thermal model and the measured values being within the acceptable range, making the model also accurate and credible.

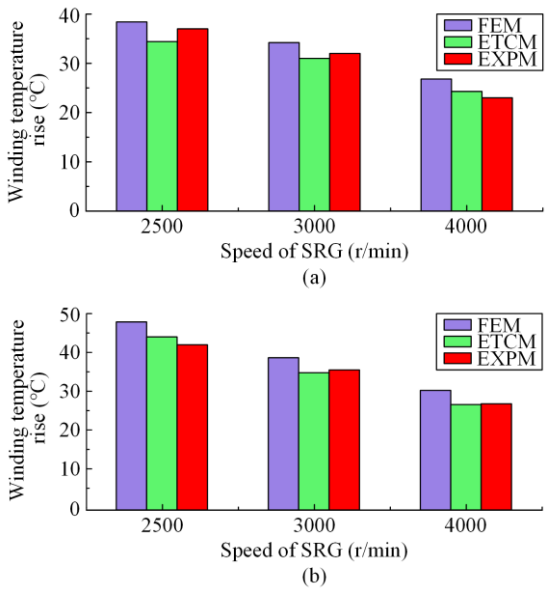

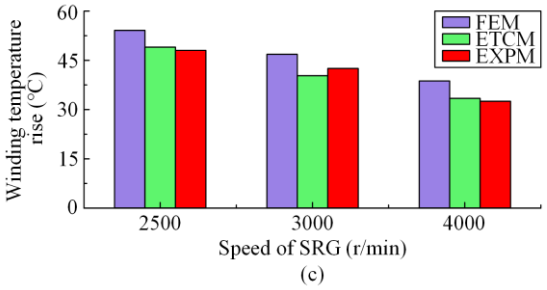

Fig. 32. Comparison results of winding temperature rise. (a) 30°–57°. (b) 30°–60°. (c) 27°–60°.

VII. Conclusion

Many research achievements on switched reluctance drive motors for electric vehicles have been made, but studies on the temperature rise of SRM used for the power generation of hybrid electric vehicles are limited. In this paper, the overall dynamic simulation model of SRG is established according to its working principles and basic equations. On the basis of the SRG transient magnetic flux density solution results, an improved variable coefficient three-term loss separation calculation model is used to calculate the iron loss heat source of SRG. Subsequently, the finite element thermal model and the equivalent thermal circuit model are used to calculate the temperature rise of each part of SRG, and the temperature rise values obtained by the two simulation models are relatively close. Meanwhile, a water-cooled structure that can directly cool the SRG windings is designed in this paper, which results in better cooling effect. Finally, an experimental platform is built to measure the temperature rise of the SRG windings. The comparison results between the experiments and the simulations also verify the accuracy of the SRG finite element thermal model and the equivalent thermal circuit model established in this paper.

Acknowledgment

Not applicable.

Authors' Contributions

Hao Chen: full-text writing and innovative points proposing. Yongqiang Liu: guidance on article structure. Fan Yang: software and simulations. Xing Wang: data collection. Zefu Tan: data preprocessing. Li Cai: complete revision. Antonino Musolino: English improvement and construction of the paper framework. Qian Huang: experimental guidance. Yong Qi: format adjustment. Guanjun Wang: experimental assistance. Lijun Xu: English improvement. Kai Ge: improvement of experimental methods. Yokub Tairov: simulation guidance. Murat Shamiyev: result interpretation. All authors read and approved the final manuscript.

FUNDING

This work is supported in part by the Shenzhen Collaborative Innovation Special Plan International Cooperation Research Project (No. GJHZ20220913144400001) and the General Research Project of Shenzhen Science and Technology Plan (No. JCYJ20220818100000001).

AVAILABILITY OF DATA AND MATERIALS

Not applicable.

DECLARATIONS

Competing interests: The authors declare that they have no known competing financial interests or personal relationships that could have appeared to influence the work reported in this article.

AUTHORS' INFORMATION

Hao Chen received B.S. and Ph.D. degrees in electrical engineering from the Department of Automatic Control, Nanjing University of Aeronautics and Astronautics, Nanjing, China, in 1991 and 1996, respectively. In 1998, he became an associate professor with the School of Information and Electrical Engineering, China University of Mining and Technology, Xuzhou, China, where he has been a professor since 2001. From 2002 to 2003, he was a visiting professor at Kyungsung University, Busan, Korea. Since 2008, he has also been an adjunct professor at the University of Western Australia, Perth, Australia. He is the author of one book and has also authored more than 200 papers. He is the holder of 15 US Patents, 86 Chinese Invention Patents and 6 Chinese Utility Model Patents. His current research interests include motor control, linear launcher, EVs, electric traction, servo drives, and wind power generator control.

Yongqiang Liu received the B.S. degree from the School of Electrical Engineering, Nantong University, Nantong, China, in 2019. And He received his M.S. degree in electrical engineering with the China University of Mining and Technology, Xuzhou, China, in 2022. His research interests include integrated drive systems for EVs and double-stator switched reluctance motors.

Fan Yang received his B.S. degree from the Yancheng Institute of Technology, Yancheng, China, in 2012, and he received his Ph.D. degree from China University of Mining and Technology in the school of Information and Electrical Engineering. Now he is a lecturer in Yancheng Institute of Technology, Yancheng, China. His current research interests include reliability analysis and direct torque control strategies.

Xing Wang received her B.S. degree from China University of Mining and Technology in computer science and technology and received her master's degree from China University of Mining and Technology in management engineering. Now she is the associate professor of China University of Mining and Technology, Xuzhou, China.

Zefu Tan now is a professor of Chongqing Three Gorges University. His current research interests include information technology and motor control strategy.

Li Cai now is a professor of Chongqing Three Gorges University. His current research interests include information technology and motor control strategy.

Antonino Musolino received the Ph.D. degree in electrical engineering from the University of Pisa, Pisa, Italy, in 1994. He is currently a full professor of electrical machines with the University of Pisa. He has coauthored more than 130 papers published in international journals/conferences. He holds three international patents in the field of magnetorheo-logical devices. His current research activities are focused on linear electromagnetic devices, motor drives for electric traction, and the development of analytical and numerical methods in electromagnetics.

Qian Huang now is a lecturer of Chongqing Three Gorges University. His current research interests include information technology and motor control strategy.

Yong Qi received his B.S. degree and Ph.D. degree from Nanjing University of Science and Technology. Now he is the professor of Nanjing University of Science and Technology.

Guanjun Wang now is working at Wuxi Inspection and Testing Certification Research Institute, Wuxi, Jiangsu, China.

Lijun Xu received his Ph.D. degree from Xinjiang University in Power System and Automation. Now he is the professor of Xinjiang Institute of Engineering, Urumqi, China.

Kai Ge now is working at Automotive Engineering Research institute, NAC Automotive Engineering Research Institute,Nanjing, China.

Yokub Tairov now is a professor of Tashkent State Technical University, Tashkent city, Republic of Uzbekistan.

Murat Shamiyev now is a professor of Tashkent State Technical University, Tashkent city, Republic of Uzbekistan.

REFERENCES

[1] Z. Yi, Z. Chen, and K. Yin *et al*., "Sensing as the key to the safety and sustainability of new energy storage devices," *Protection and Control of Modern Power Systems*, vol. 8, no. 1, pp. 1-22, Apr. 2023.

[2] S. Xu, H. Chen, and F. Song *et al*., "A diagnostic method for switch faults applied to an asymmetric half-bridge converter," *Protection and Control of Modern Power Systems*, vol. 10, no. 2, pp. 120-132, Mar. 2025.

[3] M. Noman, G. Li, and K. Wang *et al*., "Electrical control strategy for an ocean energy conversion system," *Protection and Control of Modern Power Systems*, vol. 6, pp. 1-18, Apr. 2021.

[4] W. Ding, "Comparative study on dual-channel switched reluctance generator performances under single- and dual-channel operation modes," *IEEE Transactions on Energy Conversion*, vol. 27, no. 3, pp. 680-688, Sept. 2012.

[5] J. H. Kim and R. Y. Kim, "Sensorless direct torque control using the inductance inflection point for a switched reluctance motor," *IEEE Transactions on Industrial Electronics*, vol. 65, Dec. 2018.

[6] A. Verma, S. S. Ahmad, and G. Narayanan, "Optimal control of single-pulse-operated switched reluctance generator to minimize RMS phase and RMS DC-bus current," *IEEE Transactions on Industry Applications*, vol. 60, no. 1, pp. 507-519, Jan. 2024.

[7] S. Song, L. Ge, and Z. Zhang, "Accurate position estimation of SRM based on optimal interval selection and linear regression analysis," *IEEE Transactions on Industrial Electronics*, vol. 63, no. 6, pp. 3467-3478, Jun. 2016.

[8] K. Seong, J. Hwang, and J. Shim *et al*., "Investigation of temperature rise in an induction motor considering the effect of loading," *IEEE Transactions on Magnetics*, vol. 50, no. 11, pp. 1-4, Nov. 2014.

[9] N. Zhao and W. Liu., "Loss calculation and thermal analysis of surface-mounted PM motor and interior PM motor," *IEEE Transactions on Magnetics*, vol. 51, no. 11, pp. 1-4, Nov. 2015.

[10] L. Mo, X. Zhu, and T. Zhang *et al*., "Temperature rise calculation of a flux-switching permanent-magnet double-rotor machine using electromagnetic-thermal coupling analysis," *IEEE Transactions on Magnetics*, vol. 54, no. 3, pp. 1-4, Mar. 2018.

[11] S. S. Ahmad, C. Urabinahatti, and K. N. V. Prasad *et al*., "High-switching-frequency SiC power converter for high-speed switched reluctance machine," *IEEE Transactions on Industry Applications*, vol. 57, no. 6, pp. 6069-6082, Nov. 2021.

[12] Y. Xia, Y. Xu, and M. Ai *et al*., "Temperature calculation of an induction motor in the starting process," *IEEE Transactions on Applied Superconductivity*, vol. 29, no. 2, pp. 1-4, Mar. 2019.

[13] X. Huang, J. Liu, and C. Zhang *et al*., "Calculation and experimental study on temperature rise of a high over Load tubular permanent magnet linear motor," *IEEE Transactions on Plasma Science*, vol. 41, no. 5, pp. 1182-1187, May 2013.

[14] G. Lian, H. Li, and B. Chen *et al*., "Characteristic analysis and temperature rise calculation of PMSM under different power supply modes," *IEEE Transactions on Applied Superconductivity*, vol. 29, no. 2, pp. 1-5, Mar. 2019.

[15] C. Yang, Y. Zhang, and H. Qiu, "Influence of output voltage harmonic of inverter on loss and temperature field of permanent magnet synchronous motor," *IEEE Transactions on Magnetics*, vol. 55, no. 6, pp. 1-5, Jun. 2019.

[16] L. Ge, B. Burkhart, and R. W. DeDoncker, "Fast iron loss and thermal prediction method for power density and efficiency improvement in switched reluctance machines," *IEEE Transacyions on Industrial Electronics*, vol. 67, no. 6, pp. 4463-4473, Jun. 2020.

[17] H. Chen, K. Wang, and W. Yan *et al*., "Temperature analysis of switched reluctance motor based on equivalent heat circuit method," *IEEE Transactions on Applied Superconductivity*, vol. 31, no. 8, pp. 1-4, Nov. 2021.

[18] W. Yan, H. Chen, and Y. Liu *et al*., "Iron loss and temperature analysis of switched reluctance motor for electric vehicles," *IET Electric Power Applications*, vol. 14, no. 11, pp. 2119-2127, Nov. 2020.

[19] P. S. Nasab, M. Moallem, and E. S. Chaharsoghi *et al*., "Predicting temperature profile on the surface of a switched reluctance motor using a fast and accurate magneto-thermal model," *IEEE Transactions on Energy Conversion*, vol. 35, no. 3, pp. 1394-1401, Sept. 2020.

[20] N. Arbab, W. Wang, and C. Lin *et al*., "Thermal modeling and analysis of a double-stator switched reluctance motor," *IEEE Transactions on Energy Conversion*, vol. 30, no. 3, pp. 1209-1217, Sept. 2015.

[21] D. M. Ionel, M. Popescu, and M. I. McGilp *et al*., "Computation of core losses in electrical machines using improved models for laminated steel," *IEEE Transactions on Industry Applications*, vol. 43, no. 6, pp. 1554-1564, Nov. 2007.

[22] D. M. Ionel, M. Popescu, and S. J. Dellinger *et al*., "On the variation with flux and frequency of the core loss coefficients in electrical machines," *IEEE Transactions on Industry Applications*, vol. 42, no. 3, pp. 658-667, May 2006.

[23] M. Zhang, Y. Han, and Y. Liu *et al*., "Multi-timescale modeling and dynamic stability analysis for sustainable microgrids: state-of-the-art and perspectives," *Protection and Control of Modern Power Systems*, vol. 9, no. 3, pp. 1-35, May 2024.